International Journal of Solids and Structures 49 (2012) 1828–1838

Contents lists available at SciVerse ScienceDirect

International Journal of Solids and Structures

journal homepage: www.elsevier.com/locate/ijsolstr

Homogenization modeling of thin-layer-type microstructures

B. Klusemann *, B. Svendsen

Material Mechanics, RWTH Aachen University, 52062 Aachen, Germany

ARTICLE INFO

Article history:
Received 9 December 2011
Received in revised form 20 March 2012
Available online 30 March 2012

Keywords:
Microstructure
Laminate
Composites
Homogenization
Viscoplasticity
Energy functional

ABSTRACT

The purpose of this paper is to introduce a homogenization method for the material behavior of two-phase composites characterized by a thin-layer-type microstructure. Such microstructures can be found for example in thermally-sprayed coating materials like WC/Fe in which the phase morphology takes the form of interpenetrating layers. The basic idea here is to idealize the thin-layered microstructure as a first-order laminate. Comparison of the methods with existing homogenization schemes as well as with the reference finite-element model for idealized composites demonstrates the advantage of the current approach for such microstructures. Further an extension of the approach to a variable interface orientation is presented. In the end the current method is compared to results based on FE-models of real micrographs.

1. Introduction

The modeling of the material behavior of composites is generally based on a model for the behavior of each constituent or phase of the composite together with one for the interaction of the phases. Traditionally, highly-idealized analytical and semi-analytical models were developed for this purpose with the help of volume-averaging or homogenization methods (e.g., Reuss, Voigt, Hashin–Shtrikmann, and so on), and are limited to linear thermoelasticity. More recently, methods for this purpose based on the assumption of scale-separation and the concept of representative volume element (RVE) have been developed and applied. These include the Mori–Tanaka method (e.g., Benveniste, 1987), the interpolative double inclusion model (e.g., Pierard et al., 2004), interaction direct derivative (IDD) method (Zheng and Du, 2001; Du and Zheng, 2002), self-consistent schemes such as the GSCS (Christensen and Lo, 1979) or higher-order bounds (Torquato and Lado, 1992). For a further overview and details see Nemat-Nasser and Hori (1993, 1999). Generally-speaking, these latter methods consist of two steps. In the first step, a local problem for a single inclusion is solved in order to obtain a model for the material behavior at the RVE-level. The prototype here is the approach of Eshelby (1957) for the case of an ellipsoidal elastic inclusion in an infinite matrix. The second step consists of averaging the RVE-fields to obtain those for the composite as a whole (e.g., Mercier and Molinari, 2009). As before, the focus here has been on linear thermoelasticity, also in order to exploit linearity in the mathematical formulation. For this case efficient methods are at hand, which are discussed, e.g., in Klusemann et al. (2012b). By analogy, extensions of these methods to the inelastic case are generally based on linearized incremental formulations (e.g., Ponte Castaneda and Suquet, 1998) pertaining mainly to metal inelasticity. The pioneer work of Sachs (1928) and Taylor (1938) can be seen as first homogenization methods for plasticity. The modification of the Sachs model by a static model (Zaoui, 1970) lead to a model which assumes that each constituent is subjected to the same stress which is equal to the macroscopic one which lead to a lower bound for the effective behavior. In the Taylor model uniform plastic strains are assumed which are equal to the macroscopic ones which lead to a upper bound. Dvorak (1992) proposed the so called transformation field analysis (TFA) in which the plastic strain fields were assumed to be phase-wise constant to calculate the effective behavior of inelastic composite materials (see also Dvorak et al., 1994a,b). As discussed by, e.g., Molinari et al. (1997), many of these approaches neglect the interactions between the phases, something which results in too stiff behavior. Because of this, models were developed which take phase interaction into account in some fashion (e.g., Molinari et al., 1987; Lebensohn and Tome, 1993). Michel and Suquet (2003, 2004) modified the transformation field analysis to account for spatially heterogeneous plastic strain fields resulting, e.g., from the interaction between the phases, which is named nonuniform transformation field analysis. They applied these methods mainly to composites with elastic–plastic phases. This method was studied further by several authors. For example, Roussette et al. (2009) applied it to elastic–viscoplastic constituents, and Fritzen and Böhlke (2011) analyzed the effect of different particle morphology in a metal-matrix composite with this method. Originally the nonuniform transformation field analysis was

* Corresponding author. Fax: +49 241 80 92007.
E-mail address: benjamin.klusemann@rwth-aachen.de (B. Klusemann).

0020-7683/$ - see front matter © 2012 Elsevier Ltd. All rights reserved.
http://dx.doi.org/10.1016/j.ijsolstr.2012.03.027

used in combination with a fast fourier transform (FFT) framework (Moulinec and Suquet, 1998). An implementation into the finite element framework is given by Fritzen and Böhlke (2010). Recently Agoras and Ponte Castañeda (2011) presented a generalization to multi-scale systems of the "variational linear comparison" method of Ponte Castañeda (1991) which allows the conversion from classical bounds or estimates for linear material behavior to nonlinear material behavior. A fully computational approach which is getting more popular in recent times is the use of FE^2 techniques (e.g., Smit et al., 1998; Miehe et al., 1999; Feyel, 2003). An overview about this topic was given by Geers et al. (2010).

In general the direct computation of the effective properties is based on an RVE which is the smallest unit of material, which fully describes the material behavior. The determination of the minimum RVE size is a non-trivial task. Drugan and Willis (1996) and Monetto and Drugan (2004, 2009) presented approaches to obtaining the minimum size by a non-local approach. Kanit et al. (2003) studied the necessary RVE size for random microstructure not only with respect to the wanted precision but also with the number of realization of a given microstructure volume.

If the RVE is very small or the characteristic size of the system approaches that of the microstructure, size effects can occur (e.g., Fülöp et al., 2006; Klusemann et al., 2012d), which are not accounted for at the macroscale. Furthermore, large spatial gradients at the macro-scale cannot be resolved by these methods and they are in general restricted to standard continuum mechanics theory. Full extension to second-order to incorporate size-effects of the underlying microstructure can be found by several authors (e.g., Kouznetsova et al., 2004; Bargmann et al., 2010; Klusemann, 2012a). Describing local deformation state of microstructured materials by extended continuum theories is done (e.g., Forest, 2008; Jänicke et al., 2009). In other cases, (e.g., Böhlke et al., 2008) texture related microstructural effects are accounted for by using orientation distribution functions and texture coefficients to predict the resulting anisotropy in sheet metals and the path-dependent mechanical properties. Houtte et al. (2005) presented an advanced Taylor-type statistical multi-grain model (ALAMEL) which accounts for the interactions between neighboring grains which is used to calculate the deformation texture in cubic metals.

The purpose of the current work is to present a homogenization approach for two-phase composites whose microstructure is characterized by being layer- or lamellar-like (laminate model). Such microstructures are present for example in thermally-sprayed coatings. The layered phase morphology arising here is determined among other things by the nature of the manufacturing process. The current homogenization strategy is based on the idealization of such microstructure as first-order laminate (e.g., Silhavy, 1997; Ortiz et al., 2000). This kind of idealization is used in the literature for different applications.

Ahzi et al. (1995) proposed a method to estimate the overall elastic properties of semi-crystalline polymers showing a layered structure. In Ahzi et al. (2007) three approaches are presented to determine the effective elastic properties of such structure by using a two-phase inclusion model with a crystalline lamella and amorphous domain connected over a planar interface as the local representative element of the polymer. Viscoplastic Taylor-type models have been used by, for example, Parks and Ahzi (1990); Ahzi et al. (1990) and Lee et al. (1995) for the prediction of texture evolution for a semi-crystalline polymeric material with a layered structure. In this context formulated Lee et al. (1993a,b) a rigid-viscoplastic inclusion model. van Dommelen et al. (2003) extended this model to an elasto-viscoplastic formulation which is used to determine the deformation and texture evolution of semi-crystalline polymers under loading. In Lee et al. (2002) bicrystal-based averaging schemes are presented for modeling the behavior of polycrystals for rigid viscoplasticity at large deformations. In this work the local homogenization is achieved by volume-averaging the bicrystal and considering the jump conditions at the planar interface between the two crystals assumed as occurring in a layered structure. Ortiz et al. (2000) used the idea of laminates for the description of the evolution of microstructures which show lamellar dislocation structures at large strains under monotonic loading. In this work the microstructure is idealized as first-order laminate. Furthermore models based on the idealization of first-order laminates are used for the transformation interface between, e.g., austenite and martensite in the realm of phase transformations (e.g., Kouznetsova et al., 2009). One main difference to most previously mentioned approaches is the used energy approach in this work.

The paper begins in Section 2 with a brief summary of the viscoplastic material model for each phase of the two-phase composite under consideration. The current approach as based on first-order laminate theory is introduced in Section 3. After investigating the behavior of this model with the help of simple deformation cases together with corresponding FE results for layered composites in Section 4, a comparison of results from the laminate model with analogous ones from selected existing homogenization models (e.g., Taylor, phase-wise constant plastic deformation) is given in Section 5. Followed by a discussion of a variable interface direction in Section 6. Next in Section 7 the creation of FE-models based on real micrographs and comparison to the current homogenization approach are discussed. The work ends (Section 8) with a summary and conclusions. For simplicity, the current work is restricted to small deformation.

2. Material model

In the current work, material models are formulated in the context of continuum thermodynamics. In this context, the material behavior is related to energetic and dissipative processes. As usual, the energetic part is determined by the free energy density ψ. For simplicity, attention is restricted here to quasi-static conditions and metallic materials exhibiting small deformation and Voce (i.e., saturation) isotropic hardening. In this case, the additive form

$$\psi(\boldsymbol{E}_{\mathrm{E}}, \alpha_{\mathrm{P}}) = \frac{1}{2}\boldsymbol{E}_{\mathrm{E}} \cdot \mathcal{C}_{\mathrm{E}}\boldsymbol{E}_{\mathrm{E}} + s_{\mathrm{H}}\left\{\alpha_{\mathrm{P}} + \frac{1}{c_{\mathrm{H}}}(e^{-c_{\mathrm{H}}\alpha_{\mathrm{P}}} - 1)\right\} \tag{1}$$

of ψ into elastic and hardening contributions, respectively, is assumed. In particular, the former depends on the elastic strain

$$\boldsymbol{E}_{\mathrm{E}} = \boldsymbol{E} - \boldsymbol{E}_{\mathrm{P}}, \tag{2}$$

corresponding inelastic strain $\boldsymbol{E}_{\mathrm{P}}$, and total (small) strain $\boldsymbol{E} = \mathrm{sym}(\boldsymbol{F} - \boldsymbol{I})$, with $\boldsymbol{F}$ the deformation gradient. Here, $\mathrm{sym}(\boldsymbol{A}) := \frac{1}{2}(\boldsymbol{A} + \boldsymbol{A}^{\mathrm{T}})$, represents the symmetric part of any second-order tensor $\boldsymbol{A}$. The evolution of $\boldsymbol{E}_{\mathrm{P}}$ depends on that of the accumulated equivalent inelastic deformation α_{P}, as shown in (6) below. Material properties here include the elastic stiffness tensor $\mathcal{C}_{\mathrm{E}}$, the difference s_{H} between the initial and saturated values of the yield stress, and the rate c_{H} of hardening saturation. As usual, the free energy determines in particular the stress

$$\boldsymbol{T} = \partial_{\boldsymbol{E}_{\mathrm{E}}}\psi. \tag{3}$$

Assuming dislocation glide as the dominant mechanism of inelastic deformation, the inelastic behavior is determined by an inelastic potential ϕ_{P} modeled by the simple viscoplastic form

$$\phi_{\mathrm{P}}(\varsigma_{\mathrm{P}}) = \sigma_{\mathrm{D}}\dot{\alpha}_{\mathrm{r}}\left\{\exp\left(\frac{\langle\varsigma_{\mathrm{P}} - \sigma_{\mathrm{A}}\rangle_{+}}{\sigma_{\mathrm{D}}}\right) - \frac{\langle\varsigma_{\mathrm{P}} - \sigma_{\mathrm{A}}\rangle_{+}}{\sigma_{\mathrm{D}}}\right\} \tag{4}$$

for the activation of dislocation motion and inelastic deformation. Here, $\langle f\rangle_{+} := \frac{1}{2}(f + |f|)$ represents the ramp function. In particular, this potential determines the flow rule

$$\dot{\alpha}_{\mathrm{P}} = \partial_{\langle\varsigma_{\mathrm{P}} - \sigma_{\mathrm{A}}\rangle_{+}}\phi_{\mathrm{P}} \tag{5}$$

for α_P. Here, σ_A is the initial activation (yield) stress, σ_D represents the drag stress, and $\dot{\alpha}_r$ is the characteristic deformation rate associated with dislocation motion. In addition, $\varsigma_P = \sigma_{vM} - \partial_{\alpha_P}\psi$ is the thermodynamic conjugate to α_P for the current model, where $\sigma_{vM}(\boldsymbol{T}) = \sqrt{3\mathrm{dev}(\boldsymbol{T})\cdot\mathrm{dev}(\boldsymbol{T})/2}$ represents the von Mises equivalent stress measure. Here, $\mathrm{dev}(\boldsymbol{A}) := \boldsymbol{A} - \frac{1}{3}\mathrm{tr}(\boldsymbol{A})\boldsymbol{I}$ represents the deviatoric part, and $\mathrm{tr}(\boldsymbol{A})$ the trace, of any second-order tensor $\boldsymbol{A}$. The evolution of $\boldsymbol{E}_P$ is assumed to be activated by that of α_P. Consider in this regard the constitutive relation

$$\dot{\boldsymbol{E}}_P = \dot{\alpha}_P \boldsymbol{N}_P \tag{6}$$

for the evolution of $\boldsymbol{E}_P$ quasi-linear in $\dot{\alpha}_P$, with $\boldsymbol{N}_P = \partial_{\boldsymbol{T}}\sigma_{vM}(\boldsymbol{T})$ the flow direction. Here we have assumed that the deformation is small enough so that no significant grain rotation and no texture development takes place.

For simplicity, the inelastic homogenization models to be considered in what follows are based on the following explicit algorithm. This is formulated on an arbitrary time interval $[t_n, t_{n+1}]$ of duration $t_{n+1,n} := t_{n+1} - t_n$. The algorithm begins with the forward-Euler update

$$\alpha_{Pn+1,n} = \begin{cases} 0 & \varsigma_{Pn} \leqslant \sigma_A \\ t_{n+1,n}\dot{\alpha}_r\left\{\exp\left(\frac{\varsigma_{Pn}-\sigma_A}{\sigma_D}\right) - 1\right\} & \varsigma_{Pn} > \sigma_A \end{cases} \tag{7}$$

for α_P from (5), with $\alpha_{Pn+1,n} := \alpha_{Pn+1} - \alpha_{Pn}$. In turn, this induces the update

$$\boldsymbol{E}_{En+1} = \boldsymbol{E}_{n+1} - \boldsymbol{E}_{Pn+1} = \boldsymbol{E}_{n+1} - \boldsymbol{E}_{Pn} - \alpha_{Pn+1,n}\boldsymbol{N}_{Pn} \tag{8}$$

of the elastic strain, and so that

$$\boldsymbol{T}_{n+1} = \mathcal{C}_E[\boldsymbol{E}_{En+1}] \tag{9}$$

of the stress. Consequently, the history variables for each phase include α_P and $\boldsymbol{E}_P$ here.

The above model contains the material properties $\mathcal{C}_E$, s_H, c_H, σ_A, σ_D, and $\dot{\alpha}_r$, which are to be specified for each phase in what follows. This completes the short summary of the material model for each phase. Now we turn to the homogenization scheme of interest in this work.

The homogenization approach to be discussed in what follows is based as usual on the assumption of scale separation, which lies at the heart of the RVE concept. From the numerical point of view, this facilitates the restriction of microstructural effects on the material behavior to the integration-point level of a corresponding finite-element simulation. In the current purely mechanical incremental inelastic context, this involves as usual the specification of deformation gradients $\boldsymbol{F}_n$ and $\boldsymbol{F}_{n+1}$ at the beginning ($t = t_n$) and end ($t = t_{n+1}$) of the current time interval $[t_n, t_{n+1}]$, as well as the values α_{Pn} and $\boldsymbol{E}_{Pn}$ of the internal variables at the beginning of this interval. In this case, the total strain $\boldsymbol{E}_n = \mathrm{sym}(\boldsymbol{F}_n - \boldsymbol{I})$ and $\boldsymbol{E}_{n+1} = \mathrm{sym}(\boldsymbol{F}_{n+1} - \boldsymbol{I})$ at the beginning and end of this interval, respectively, are specified.

3. Laminate model

As discussed in the introduction, layer or laminate-like microstructures arise in technological processes such as thermal spraying. Both from this point of view, and as an alternative means to model the interaction of the phases in a composite with the corresponding morphology, it is interesting to formulate the corresponding homogenization model and compare it with selected existing ones for the inelastic case. For simplicity, attention is restricted here to the case of small deformation. For the case of micron-thick thermal spray coatings, for example, this assumption is certainly reasonable. In this case, the kinematics of the two-phase system is determined by the mixture relation

$$\boldsymbol{F} = \lambda\boldsymbol{F}_1 + (1-\lambda)\boldsymbol{F}_2 = \boldsymbol{F}_2 + \lambda[\![\boldsymbol{F}]\!] \tag{10}$$

for the deformation gradient $\boldsymbol{F}$, where $[\![f]\!] = f_1 - f_2$ represents the "jump" of f across the phase interface. In particular, in the laminate context (e.g., Silhavy, 1997), the jump $[\![\boldsymbol{F}]\!]$ in deformation state across the phase interface is modeled constitutively via the rank-one connection

$$[\![\boldsymbol{F}]\!] = \boldsymbol{h}\otimes\boldsymbol{m} \tag{11}$$

determined by the interface deformation vector $\boldsymbol{h}$ and interface unit normal $\boldsymbol{m}$. In this case, note that $\boldsymbol{h} = [\![\boldsymbol{F}]\!]\boldsymbol{m}$ and $[\![\boldsymbol{F}]\!](\boldsymbol{I} - \boldsymbol{m}\otimes\boldsymbol{m}) = \boldsymbol{0}$ hold at the interface. This is only valid due to the assumption of a zero-thickness interface between the two phases. Solving (10) and (11) for $\boldsymbol{H}_i = \boldsymbol{F}_i - \boldsymbol{I}$, $i = 1, 2$, we obtain

$$\begin{aligned} \boldsymbol{H}_1(\boldsymbol{H}, \lambda, \boldsymbol{h}, \boldsymbol{m}) &= \boldsymbol{H} + (1-\lambda)\boldsymbol{h}\otimes\boldsymbol{m}, \\ \boldsymbol{H}_2(\boldsymbol{H}, \lambda, \boldsymbol{h}, \boldsymbol{m}) &= \boldsymbol{H} - \lambda\boldsymbol{h}\otimes\boldsymbol{m}, \end{aligned} \tag{12}$$

with the mixture displacement gradient $\boldsymbol{H} = \boldsymbol{F} - \boldsymbol{I}$. In turn, these yield the corresponding strains

$$\begin{aligned} \boldsymbol{E}_1(\boldsymbol{E}, \lambda, \boldsymbol{h}, \boldsymbol{m}) &= \boldsymbol{E} + (1-\lambda)\mathrm{sym}(\boldsymbol{h}\otimes\boldsymbol{m}), \\ \boldsymbol{E}_2(\boldsymbol{E}, \lambda, \boldsymbol{h}, \boldsymbol{m}) &= \boldsymbol{E} - \lambda\,\mathrm{sym}(\boldsymbol{h}\otimes\boldsymbol{m}), \end{aligned} \tag{13}$$

as functions of the mixture strain $\boldsymbol{E}$, the volume fraction λ of phase 1, and the interface properties $\boldsymbol{h}$ and $\boldsymbol{m}$. Like the deformation and strain, the free energy density of the mixture is modeled as a volume-fraction-weighted convex combination

$$\begin{aligned} \psi(\boldsymbol{E}, \lambda, \boldsymbol{h}, \boldsymbol{m}, \boldsymbol{E}_{P1}, \alpha_{P1}, \boldsymbol{E}_{P2}, \alpha_{P2}) = \lambda\psi(\boldsymbol{E}_1(\boldsymbol{E}, \lambda, \boldsymbol{h}, \boldsymbol{m}) - \boldsymbol{E}_{P1}, \alpha_{P1}) \\ + (1-\lambda)\psi(\boldsymbol{E}_2(\boldsymbol{E}, \lambda, \boldsymbol{h}, \boldsymbol{m}) \\ - \boldsymbol{E}_{P2}, \alpha_{P2}) \end{aligned} \tag{14}$$

of the corresponding phase quantities, with ψ given by (1). In this case, we neglect any additional possible contributions, e.g., coming from the interface itself. In these relations, the total strain $\boldsymbol{E}$ is given, and the phase quantities $\boldsymbol{E}_{P1,2}$ and $\alpha_{P1,2}$ are determined by the evolution-constitutive relations (5) and (6), respectively. This leaves λ, $\boldsymbol{h}$ and $\boldsymbol{m}$ as independent constitutive variables in the model yet to be determined. In particular, since λ is basically determined by the technological process and known, we model it as constant here. In addition, we begin by assuming that the orientation $\boldsymbol{m}$ of the laminate interface is fixed and parallel to the thickness direction of the coating/composite. To determine $\boldsymbol{h}$, we assume that it is purely energetic in nature and require its value to satisfy mechanical equilibrium

$$\boldsymbol{0} = \partial_{\boldsymbol{h}}\psi = \lambda(1-\lambda)[\![\boldsymbol{T}]\!]\boldsymbol{m} \tag{15}$$

at the interface ($\lambda \neq 0$). This yields an implicit equation for $\boldsymbol{h}$. A related deformation-gradient based framework was used by Ortiz et al. (2000) to describe the evolution of dislocation structures under monotonic strains in the microstructure of Al–Cu alloys.

On this basis, we can use the following algorithm to solve the model relations formulated as follows. As already stated above, for the current time-step, $\boldsymbol{E}_n = \mathrm{sym}(\boldsymbol{F}_n - \boldsymbol{I})$ and $\boldsymbol{E}_{n+1} = \mathrm{sym}(\boldsymbol{F}_{n+1} - \boldsymbol{I})$ are known. In addition, $\boldsymbol{h}_n$, $\boldsymbol{E}_{P1\,n}$, $\alpha_{P1\,n}$, $\boldsymbol{E}_{P2\,n}$, and $\alpha_{P2\,n}$ are known. From the explicit update of the inelastic phase variables outlined in Section 2, we then have $\alpha_{P\omega\,n+1}$ and $\boldsymbol{E}_{P\omega\,n+1}$. Using these, one can then calculate

$$\begin{aligned} \boldsymbol{E}_{E\omega\,n+1}(\boldsymbol{h}) &= \boldsymbol{E}_{\omega\,n+1}(\boldsymbol{E}_{n+1}, \boldsymbol{h}) - \boldsymbol{E}^{\omega}_{Pn+1}, \\ \boldsymbol{T}_{\omega\,n+1}(\boldsymbol{h}) &= \mathcal{C}_{E\omega}\boldsymbol{E}_{E\omega\,n+1}(\boldsymbol{h}), \end{aligned} \tag{16}$$

and so solve (15) for $\boldsymbol{h}_{n+1}$. A convergence study for the number of iteration steps for the solution of $\boldsymbol{h}$ was carried out. The exact solution was defined for a deviation of 10^{-12} between $\boldsymbol{h}_{n+1}$ and $\boldsymbol{h}_n$. It was found that after one iteration step the deviation between this value and the exact solution is less than 0.1%. Therefore only one iteration

step is necessary. Given $\boldsymbol{h}_{n+1}$ and the corresponding current phase stresses $\boldsymbol{T}_{1\,n+1}$ and $\boldsymbol{T}_{2\,n+1}$, (9) determines the current composite stress, and

$$\begin{aligned}\partial^{\mathrm{a}}_{\boldsymbol{E}_{n+1}}\boldsymbol{T}_{n+1} &= \lambda\,\partial^{\mathrm{a}}_{\boldsymbol{E}_{n+1}}\boldsymbol{T}_{1\,n+1} + (1-\lambda)\,\partial^{\mathrm{a}}_{\boldsymbol{E}_{n+1}}\boldsymbol{T}_{2\,n+1}\\ &= \lambda\left\{\partial_{\boldsymbol{E}_{n+1}}\boldsymbol{T}_{1\,n+1} + (\partial_{\boldsymbol{h}_{n+1}}\boldsymbol{T}_{1\,n+1})(\partial^{\mathrm{a}}_{\boldsymbol{E}_{n+1}}\boldsymbol{h}_{n+1})\right\}\\ &\quad + (1-\lambda)\left\{\partial_{\boldsymbol{E}_{n+1}}\boldsymbol{T}_{2\,n+1} + (\partial_{\boldsymbol{h}_{n+1}}\boldsymbol{T}_{2\,n+1})(\partial^{\mathrm{a}}_{\boldsymbol{E}_{n+1}}\boldsymbol{h}_{n+1})\right\},\end{aligned} \tag{17}$$

the corresponding stress tangent, where a denotes the total derivative.

4. Model behavior

To apply the laminate model to a given microstructure, the volume fraction λ of phase 1 and normal direction $\boldsymbol{m}$, which are considered fixed and known here in the case of manufactured composites, have to be chosen. In general, these could be chosen arbitrarily. On the other hand, in the case of thin coatings, the layered microstructure has a normal direction approximately parallel to the thickness direction of the coating, as shown in Fig. 1. As discussed in Section 2, we investigate the laminate model for a composite consisting of isotropic, thermoelastic, viscoplastic phases, one being soft and the other hard. This is roughly analogous to the case of WC–FeCSiMn coatings shown in Fig. 1. The parameter values chosen for the two phases are given in Table 1. In addition, $\dot{\alpha}_{\mathrm{r}}$ is fixed at $10^{-3}\,\mathrm{s}^{-1}$, corresponding to quasi-static loading conditions.

Realistically speaking, we should model a hard ceramic phase like WC as thermoelastic and brittle. For simplicity, however, we restrict attention to a model microstructure in which the hard phase is modeled as being thermoelastic and ideal viscoplastic. In particular, for lack of more specific information, the value of σ_{A} for the hard phase was set equal to the maximum strength of WC/Co at low cobalt content (e.g., Han and Mecholsky, 1990; Okamoto et al., 2005).

Consider next the behavior of the model for this microstructure with the help of the following four deformation conditions: (i) F_{33}-extension parallel to the layers, (ii) F_{11}-compression parallel to $\boldsymbol{m}$, (iii) F_{21}-shear parallel to the layers, and (iv) F_{23}-shear of both phases parallel to the interface. These are shown schematically in Fig. 2. The applied deformation rate for all following simulation is $10^{-3}\,\mathrm{s}^{-1}$ representing a quasi-static loading.

Below, we will investigate the stress–strain response of the composite subject to these four deformation conditions predicted by different homogenization methods, including the current laminate-based one. Before doing this, we first investigate the behavior of the laminate model using single-element calculations.

To this end, uniform displacement boundary conditions are applied. For the extension and compression case these are accomplished by applying the displacement to the corresponding face and fixing the three faces connected to the point in the bottom right in their respective normal directions (bottom in 1, back in 2 and right in 3). The further direction and faces are traction free. For the shear case. the displacement is applied to the corresponding face and direction and the remaining direction of this face and the direction of the face on the opposite site of the element are fixed.

We begin with cases (i) and (ii), i.e., F_{33}-extension parallel to the layers, and F_{11}-compression parallel to $\boldsymbol{m}$, respectively. The corresponding results are shown in Fig. 3. The shown macroscopic von Mises stress is the von Mises stress of the macroscopic stress tensor $\sigma_{\mathrm{vM}}(\boldsymbol{T})$ calculated via the mixture rule $\boldsymbol{T} = \lambda\boldsymbol{T}_1 + (1-\lambda)\boldsymbol{T}_2$.

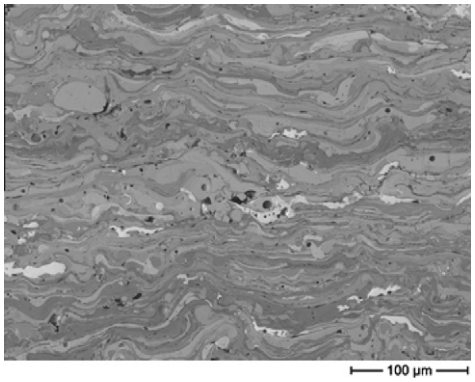

Fig. 1. Example of a layered microstructure in an arc sprayed WC–FeCSiMn coating which has been thermally sprayed at 700 K onto a steel (Ck45) substrate at room temperature. The different phases in the coating (WC and FeCSiMn) can be distinguished due to their different densities which are shown in different brightness coming from regions with atoms having different atomic numbers (FeCSiMn darker than WC). Note that the normal direction to the interface between layers is on average more or less parallel to the thickness direction of the coating, which corresponds to the vertical direction in the figure.

Table 1
Material properties of the two phases in the model microstructure. $\sigma_{\mathrm{D}} = 10$ MPa and $\dot{\alpha}_{\mathrm{r}} = 0.001\mathrm{s}^{-1}$ are for both phases the same.

Material	E [GPa]	ν [–]	σ_{A} [MPa]	s_{H} [MPa]	c_{H} [–]
Soft	210	0.3	130	240	10
Hard	430	0.19	2000	0	0

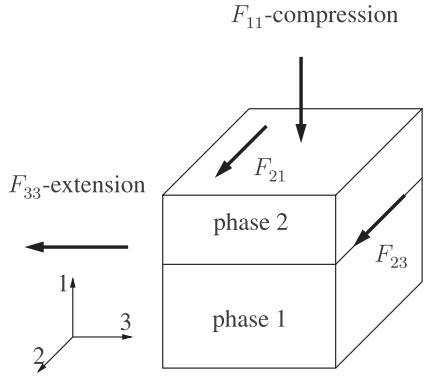

Fig. 2. Deformation conditions for investigation of the composite behavior.

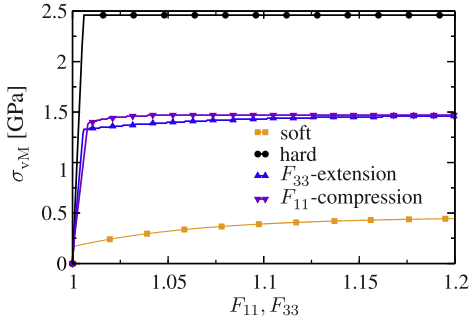

Fig. 3. Macroscopic von Mises stress σ_{vM} in the composite subject to different normal deformation conditions as a function of F_{11} (compression) or F_{33} (extension) for soft-phase volume fraction of $\lambda = 0.5$. Also shown for comparison is the behavior of the pure hard (solid circles) and pure soft (solid squares) for either extension or compression.

As shown here, the soft phase (solid squares) is almost immediately inelastic, whereas the hard phase (solid circles) has a more pronounced elastic range. Note that the elastic-inelastic transition for F_{33}-extension takes place in the composite almost at the same deformation state as in the hard phase alone, numerically 4% later. On the other hand, this transition is displaced to more than 15% larger deformation in the F_{11}-compression case. As deformation proceeds in the inelastic range, the stress–strain response of the composite for these two cases converges. Mechanical equilibrium requires the normal traction at the interface to be continuous. Because of this, the elastic and inelastic strengthening effect of the hard phase is slightly more pronounced in the F_{11}-compression perpendicular to the interface than in F_{33}-extension parallel to the interface.

Consider next the development of the normal $(\boldsymbol{h}\cdot\boldsymbol{m})\boldsymbol{m}$ component of $\boldsymbol{h}$ at the interface during extension and compression deformation as shown in Fig. 4. Relative to the coordinate system in Fig. 2, note that $\boldsymbol{h}\cdot\boldsymbol{m} = [\![F_{11}]\!]$ holds. In addition, note that $[\![F_{22}]\!] = -[\![F_{33}]\!]$ follows from continuity of the tangential deformation state at the interface. Consequently, as exhibited in Fig. 4, $\boldsymbol{h}\cdot\boldsymbol{m}$ is much larger in F_{11}-compression than in F_{33}-extension. After transition to the inelastic regime, $\boldsymbol{h}\cdot\boldsymbol{m}$ decreases slightly due to hardening in the soft phase.

The behavior in the case of shear is different than for extension–compression. In particular, for the F_{23}-shear case, the results seem to be quite similar to those observed in the extension–compression case. In this case, the interface lies in the shear plane, and both phases are loaded equally. Because of this, the resulting behavior is equivalent to the behavior of the Taylor model (Taylor, 1938). On the other hand, in F_{21}-shear case, the laminate model shows completely different behavior. As shown in Fig. 5, F_{21}-shear is dominated by the behavior of the soft phase. The stress–strain curve of the composite is nearly coincident with the curve for the soft material. This result is quite similar to the behavior of the Sachs model (Sachs, 1928).

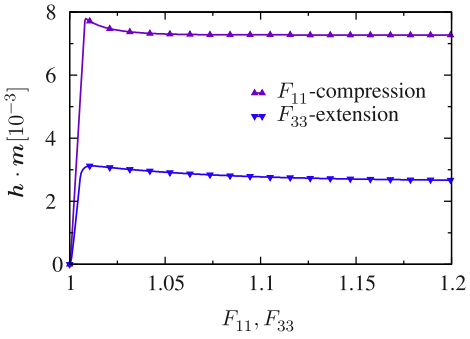

Fig. 4. Relative normal deformation $\boldsymbol{h}\cdot\boldsymbol{m}$ across the interface for F_{11}-compression and F_{33}-extension at $\lambda = 0.5$.

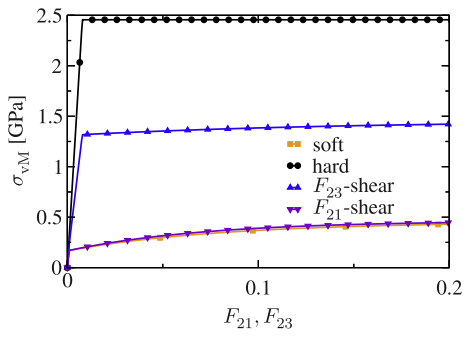

Fig. 5. Macroscopic von Mises stress σ_{vM} in the composite subject to different shear deformation conditions as a function of strain in the form of displacement u divided by length l for soft-phase volume fraction of $\lambda = 0.5$. See text for details.

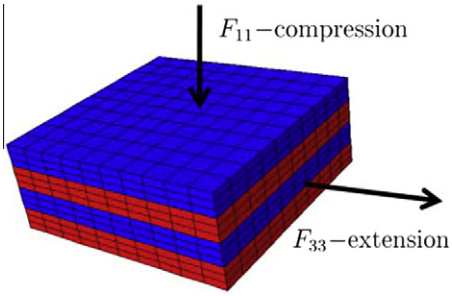

Fig. 6. FE-model for laminate for $\lambda = 0.5$ with applied loading cases (red (bottom) = soft phase, blue (top) = hard phase). (For interpretation of the references to color in this figure legend, the reader is referred to the web version of this article.)

The externally applied strain leads to large deformation of the softer phase while the hard phase undergoes only small deformation due to a nearly-uniform stress distribution. Before comparing different homogenization approaches below, a verification of the laminate model will be carried out with the help of the FE-model shown in Fig. 6. The FE model consists of layers of hexahedral finite elements of the type C3D8 with 8 integration points where the different layers are tied together. To verify that the response of the structural model is not influenced by boundary effects the comparison between the FE model (where the laminate is modeled explicitly, see Fig. 6) and the laminate model is done on the structural FE model. In this regard, the results for the laminate model are obtained from the structural model by applying the same material parameters in both layers. The finite material model used for the structural laminate model can be seen in Section 2.

In contrast to the single element test, displacement boundary conditions are applied in such a fashion that material flow which would otherwise lead to formation of bulges at the faces is prevented. This reflects that in a real compression experiment, e.g. formation of a bulge due to material flow would be prevented for interior regions by surrounded material. For the F_{11}-compression loading case the following boundary conditions are applied: the bottom face is fixed in 1-direction, the back face in 2-direction and the left face in 3-direction. Additionally the displacement for the front and the right face is restricted to be equal in both faces for 2- and 3-direction, respectively, which is guaranteed by introducing a reference point for these two faces and coupling of each face to the corresponding reference point. These boundary conditions guarantee that the deformation conditions considered lead to homogeneous deformation in every phase. For the F_{33}-extension loading case the same boundary conditions are applied with the change that now the displacement on the right face in 3-direction is given and that the top face is traction free. Fig. 7 shows the resulting stress–strain curves for the FE-model and laminate model. Additionally the local behavior of the soft phase is exemplarily shown in Fig. 8. As stated above the resulting behavior of the laminate here is mainly influenced by the different behavior of the soft phase under the different loading condition due to the ideal viscoplastic behavior of the hard phase. From both comparisons it can be seen that the behavior of FE model and the laminate model agrees quite well, i.e., in the case of homogeneous deformation.

Consider next inhomogeneous conditions. These are relevant for example to the technological case of compaction of the coating via incremental forming methods. Related to this is the material testing of such coatings with the help of indentor tests. Consequently, consider the indentation of the coating using a spherical

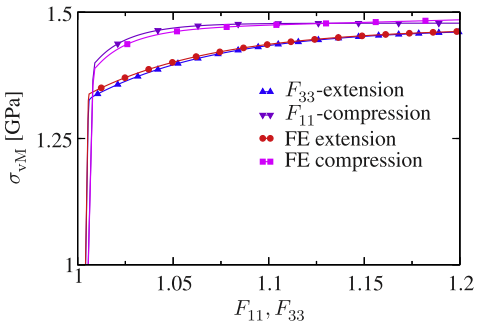

Fig. 7. Comparison between the FE model and the laminate model for $\lambda = 0.5$. Both models show the same behavior under the applied loads.

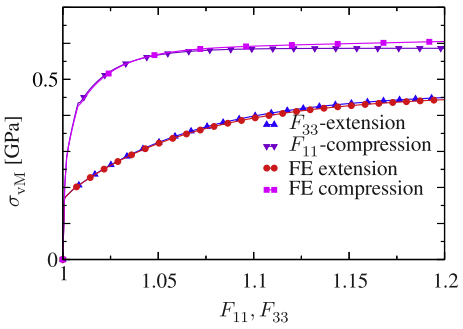

Fig. 8. Comparison between the FE model and the laminate model for the behavior of the soft phase for $\lambda = 0.5$. Both models show the same behavior under the applied loads.

indentor. Since we expect ideal RVE-related boundary conditions being employed in this work not to be completely correct in this case, the relation of the microstructural size to the indentor radius is examined here. In particular, we examine the dependence of the results on the ratio w/r of the width w of the structure to the radius r of the indentor. As this ratio increases, the boundaries are farther away from the region of loading. Consequently, the difference in the stresses predicted by the homogenization model and the FE model should decrease as this ratio increases.

The results of the indenter test are shown in Fig. 9. It is clear that the stress distribution is more homogeneous for the homogenized laminate model due to the fact that in the FE-model there is a sharp transition at the interface between the layers due to the contrast in material properties. In addition, the results as a function of w/r clearly show the decrease of boundary effects (especially near the indentor at the top) on the vertical stress distribution. As shown and as expected, the agreement improves the boundary influence decreases, i.e., as w/r increases. Except for the differences due to such boundary effects, then, we are justified in concluding that the laminate homogenization model is a reasonable "mean-field" approximation to the FE model results.

5. Comparison with other homogenization approaches

In this section, the current laminate-based homogenization model (laminate model) is compared to standard homogenization assumptions like Taylor, as well as to that of phase-wise constant plastic deformation (EPc) considered.

The assumption of phase-wise constant plastic strain is a special case of the so-called Transformation Field Analysis (TFA) proposed by Dvorak (1992). TFA offers an interesting way of reducing the number of macroscopic internal variables by assuming that phase fields are phase-wise constant. In particular, this assumption is reasonable for microstructures consisting of plastically-homogeneous domains. In general, however, it results in a model for the effective behavior of the composite which is too stiff. Indeed, this method prohibits the localization of inelastic deformation at phase boundaries as a means of stress relaxation, resulting in unrealistic stress concentration there and generally higher stresses. On the other hand, in special cases, e.g., the current one of thin layer-like composites, the relative uniformity of the stress and strain fields almost everywhere may minimize this error and lead to reasonable results. Details about the numerical implementation about the EPc method can be found in Gross and Seelig (2006) and Klusemann (2010).

To begin, consider first the compression and extension of the thin-coating-like layered microstructure from Fig. 6. Fig. 10 shows the stress–strain curves for the different homogenization methods. In the elastic range, the Taylor model agrees quite well with the laminate model in the case of extension, whereas the EPc-model agrees with the laminate model in the case of compression. In contrast to the laminate model, the EPc model exhibits the same behavior for different loading cases in the elastic range. In addition, for the chosen material parameter combination, the Taylor and EPc models show a behavior between the extension and compression response of the laminate model in the inelastic range. In particular, the yield stress of both models lies between the extremal values of the laminate model for extension and compression. With increasing deformation the Taylor model response converges to the response of the compression case of the laminate model, whereas

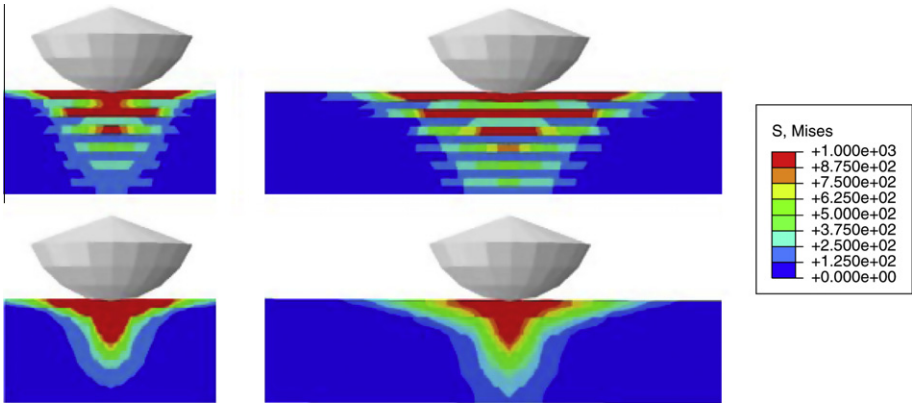

Fig. 9. Comparison of von Mises stress distribution in the structure of twelve layers (arranged as hard-soft laminate from the top) predicted by the FE model (above) and by the laminate model (below) for $w/r = 2$ (left) and $w/r = 10$ (right) with the radius $r = 6.5$ mm of the indentor, the width w and the thickness $h = 9$ mm of the structure. Although more inhomogeneous in the FE-case, the stress distribution in both cases is quite similar. As shown, with increasing w/r, better agreement is obtained.

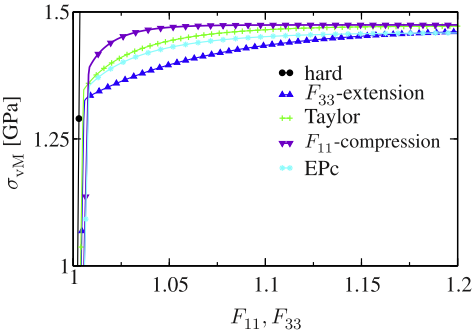

Fig. 10. Comparison of stress–strain behavior predicted by different homogenization approaches for $\lambda = 0.5$.

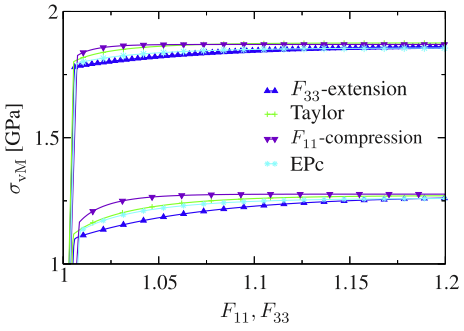

Fig. 11. Comparison of stress–strain behavior of different homogenization models for $\lambda = 0.6$ and $\lambda = 0.3$. Different homogeneous methods show analogous results as described in Fig. 10.

the EPc-model response converges to the extension case. The same behavior can also be observed for different volume fractions λ as shown in Fig. 11. Clearly, model differences are magnified upon increase of the volume fraction of the soft phase, especially in the elastic range.

The results for shear deformation are qualitatively the same as in the normal deformation cases just considered. For F_{23}-shear, in which the interface lies in the shear plane, the predictions of the laminate model and Taylor model correspond quite well. This is to be expected since, in this case, both phases experience the same deformation state (see Fig. 2). As before, for this case, the EPc model predicts softer behavior. As for the Taylor case, this is due to the fact that the material behavior is independent of loading direction for an isotropic material. For F_{21}-shear, the Taylor and EPc models predict the same behavior as before, in contrast to the behavior of the laminate model. In this case, the Sachs model would give the best prediction, but for all other loading conditions this model is absolutely inappropriate.

6. The case of variable interface orientation

For simplicity, the phase interface orientation $\boldsymbol{m}$ has been kept fixed and oriented in the direction of the coating thickness. In reality, however, there is no reason to believe that it may not vary locally in the coating during loading. To have a first look at the effect this might have on the material behavior of the composite, we now allow $\boldsymbol{m}$ to vary. For simplicity, we assume to this end that $\boldsymbol{m}$ is purely energetic and varies only in order to satisfy angular momentum at the interface, i.e.,

$$\boldsymbol{0} = \partial_{\boldsymbol{m}}\psi = \lambda(1-\lambda)[\![\partial_{\boldsymbol{F}}\psi]\!]^{\mathrm{T}}\boldsymbol{h} \tag{18}$$

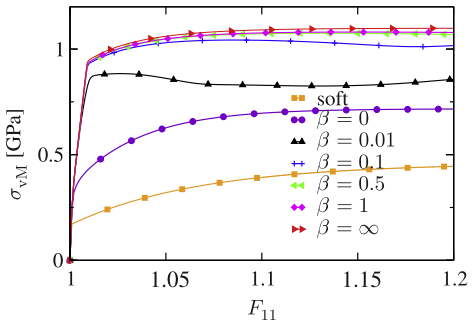

Fig. 12. Comparison of stress–strain behavior of laminate model for variable $\boldsymbol{m}$ for different values of the interface resistance $\gamma = \beta E_{\mathrm{soft}}$ under compression with $\boldsymbol{m}_0 = \{100\}$ and $\lambda = 0.7$. For comparison, the corresponding results for fixed $\boldsymbol{m} = \{100\}$ are also shown.

vanishes there in equilibrium, yielding an implicit relation for $\boldsymbol{m}$. This is of course subject to the constraint $\boldsymbol{m}\cdot\boldsymbol{m} = 1$ which is taken into account by minimizing the associated Lagrangian function

$$\ell(\boldsymbol{E}_{\mathrm{E}}, \alpha_{\mathrm{P}}, \boldsymbol{m}, \boldsymbol{h}) = \psi_{\mathrm{E}}(\boldsymbol{E}_{\mathrm{E}}, \boldsymbol{m}, \boldsymbol{h}) + \psi_{\mathrm{H}}(\alpha_{\mathrm{P}}) + \mu(\boldsymbol{m}\cdot\boldsymbol{m} - 1) \tag{19}$$

with Lagrange multiplier μ.

The values of $\boldsymbol{m}$ obtained in this fashion show that the laminate interface is reorienting to a diagonal in one plane, depending on the direction of loading as well as the initial condition. This corresponds to a reorientation of 45° for $\boldsymbol{m}_0 = \{100\}$. The corresponding stress–strain behavior ($\beta = 0$[1] is shown for compression in Fig. 12 and compared to the case of fixed interface orientation $\boldsymbol{m} = \{100\}$ ($\beta = \infty$). Since the equilibrium value of $\boldsymbol{m}$ represents energetically the most favorable orientation, it results in the lowest stress levels.

On the other hand, a reorientation of 45° of the interface for such laminates is physically unrealistic. To prevent this, we assume that the interface has a certain stiffness in the sense that reorientation beyond a certain degree is energetically unfavorable. To this end, we add a corresponding penalty term to (19), i.e.,

$$\ell(\boldsymbol{E}_{\mathrm{E}}, \alpha_{\mathrm{P}}, \boldsymbol{m}, \boldsymbol{h}) = \psi_{\mathrm{E}}(\boldsymbol{E}_{\mathrm{E}}, \boldsymbol{m}, \boldsymbol{h}) + \psi_{\mathrm{H}}(\alpha_{\mathrm{P}}) + \frac{1}{2}\gamma(1 - \boldsymbol{m}\cdot\boldsymbol{m}_0)^2 + \mu(\boldsymbol{m}\cdot\boldsymbol{m} - 1), \tag{20}$$

where γ represents the interface resistance to reorientation relative to the initial orientation $\boldsymbol{m}_0$.

First results for compression are shown in Fig. 12 for different values of the ration $\beta = \gamma/E_{\mathrm{soft}}$ of γ to Young's modulus E_{soft} of the soft phase. The corresponding development of the reorientation angle $\alpha = \arccos(\boldsymbol{m}\cdot\boldsymbol{m}_0)$ is displayed in Fig. 13. For large γ, the results agree with those for fixed $\boldsymbol{m}$ as expected. As γ decreases and the interface becomes more pliable, the stress level also decreases, again as expected. Consequently, a variable $\boldsymbol{m}$ can have a significant influence on the stress level in the composite. The question arises, is the variation of $\boldsymbol{m}$ purely energetic in nature. More generally, one could expect inelastic/kinetic/dissipative processes to influence the orientation of the interface. In this case, (18) could be generalized to

$$\boldsymbol{0} = \partial_{\boldsymbol{m}}\psi + \partial_{\dot{\boldsymbol{m}}}\chi \tag{21}$$

in terms of a dissipation potential χ depending in particular on the rate $\dot{\boldsymbol{m}}$ of interface rotation. Detailed analysis of results for variational $\boldsymbol{m}$ under different loading conditions represent ongoing research.

[1] β describes in a sense the interface stiffness and will be defined after the next text block.

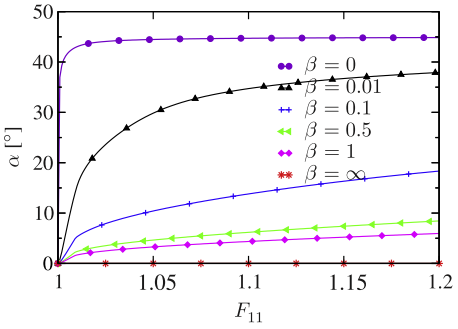

Fig. 13. Development of the reorientation angle $\alpha = \arccos(\boldsymbol{m} \cdot \boldsymbol{m}_0)$ during compression for $\boldsymbol{m}_0 = \{100\}$ and various $\gamma = \beta E_{\text{soft}}$ with $\lambda = 0.7$.

7. Comparison with discrete microstructure model

For heterogeneous materials it might be advantages to compute directly the material behavior on FE-models which use discretized microstructure images from Light Microscopy (LM) or Scanning Electron Microscopy (SEM). Such an approach was applied, e.g., by Tillmann et al. (2011) for evaluating the elastic properties and by Klusemann et al. (2012c) to analyze residual stresses in thermal sprayed coatings. In the following we will shortly summarize the generation of an FE-model of a discretized microstructure and afterwards we will compare the results to the introduced laminate homogenization approach.

7.1. Generation of FE-model from micrographs

Following Tillmann et al. (2011), as the basis for modeling the microstructure explicit micrographs from Scanning Electron Microscope (SEM) are used. SEM micrographs serve as a basis for the determination of the chemical composition of different phases. The micrograph provides the possibility to distinguish between the phases due to their different densities which are shown in different brightness coming from regions with atoms having different atomic numbers. Due to the huge difference between the relative atomic weight of tungsten (183.84 g/mol) and that of iron (55.845 g/mol), the phases of the sprayed WCFeCSiMn feature a good contrast. In addition to these two phases, pseudo-alloyed splats containing WC as well as FeCSiMn are visible which cannot be clearly identified. Here it can be distinguished between the matrix material Fe, the inclusion material WC, and pores. An exemplary micrograph is shown in Fig. 1. The differentiation between the phases is carried out using an image processing tool by finding optimal thresholds based on the color distribution, from which the different phases are separated. To make the image more feasible additional smoothing and cleanup algorithms are applied (see e.g., Jain, 1989). The generation of the FE-mesh from such an image is performed with the software Object Oriented Finite Element 2 (OOF2). OOF2 creates a FE-mesh which reflects the shape of the different phases in the microstructure with the associated material parameters. For further details about the program OOF2 see Langer et al. (2001) and Reid et al. (2008). The resulting mesh on the digitalized image is shown in Fig. 14. Due to the lamellar structure of the coating it is assumed that the microstructure would be continuous in the third dimension. Therefore the 2D mesh is extruded in the third dimension which leads to a columnar structure. In general, as shown in Wiederkehr et al. (2010) this simple extrusion leads to an incorrect result for complex structures. However, due to the lamellas (and therefore continuous structure into the third dimension) this procedure is assumed to be valid here.

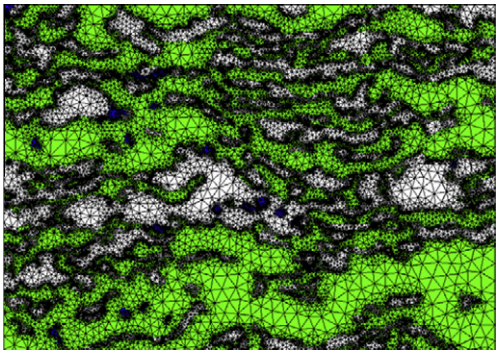

Fig. 14. Exemplary FE mesh based on digitalized image from a micrograph of WC–FeCSiMn obtained with Scanning Electron Microscopy (SEM). The mesh was generated with help of the software tool OOF2.

7.2. Comparison

In the following results from the FE model based on real micrographs are compared to the previous introduced laminate homogenization approach with respect to their macroscopic stress–strain responses. The WC phase is modeled as hard phase and the Fe phase as soft phase via the material parameters given in Table 1. The pores are assumed to have zero stiffness. Two types of boundary conditions will be used within this section. First the simulations are performed with macroscopic strain boundary conditions ('hard'), meaning that the strain on all outside surfaces is prescribed (cp., e.g., Pahr and Zysset, 2008). This leads to a nearly Taylor-like behavior. Furthermore the interface is assumed to stay nearly fixed for these boundary conditions which is considered for the laminate model by using an infinite interface stiffness. These boundary conditions lead to high hydrostatic stresses in the material which do not lead to plastic flow and are not relevant for this comparison, which is accounted for by using the von Mises stress σ_{vM} for comparison.

Fig. 15 shows the resulting stress–strain curves from the microstructural FE-model in comparison to the laminate model. The FE-model of the real microstructure shows similar behavior as the laminate model. The macroscopic stress for is obtained by averaging over the volume. First the F_{33}-real shows a stiffer behavior than the F_{11}-real, however, with increasing deformation the hardening is more pronounced for F_{11}-real. The modeling approaches show a certain deviation in the transition region from elastic to inelastic (meaning that both phases behave inelastic) where the laminate model predicts a stiffer behavior. However, in general both models show the same tendency in the behavior for the different loading directions.

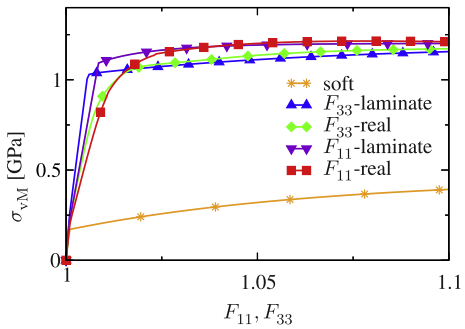

Fig. 15. Comparison of stress–strain behavior for "hard" boundary conditions of laminate model (-laminate) for fixed $m = \{100\}$ for $\lambda = 0.63$ under compression and extension with FE-model of the real microstructure (-real).

As second type of boundary conditions, 'relaxed' boundary conditions are applied which are the same as for the single-element test in Section 4. For the extension and compression case this means that the bottom face is fixed in 1, the back face in 2 and the right face in 3 and the displacement is applied to the top face in 1 (compression) and to the left face in 3 (extension) direction, respectively. This might lead to inhomogeneous deformation which can result into necking phenomena which may lead to a reorientation of the layers. An interface stiffness $\beta = 0.095$ is fitted by achieving the same stress level at 10% deformation for the laminate model as for the simulation results with real micrographs. The results are shown in Fig. 16. As a comparison the simulation results with infinite interface stiffness for F_{33} are also shown (F_{33}- m-fixed). The stress–strain results for the laminate model with variable interface orientation show a stress level which is lower compared to the simulation results for a fixed interface orientation m. For both loading directions the laminate model shows a higher yield point at the transition from elastic to inelastic behavior. Afterwards the stress is slightly decreasing for increasing deformation due to the occurring reorientation.

For 'relaxed' boundary conditions F_{33}-real shows a softer behavior than F_{11}-real except for deformation above 9%. Both loading cases show lower stress–strain curves as for 'hard' boundary conditions due to higher deformation in the Fe-phase which results from the discontinuities in the WC-lamellas. Furthermore reorientation occurs of these lamellas which also lead to necking of the specimen. This necking/reorientation also leads to a decrease in the stress at larger deformation.

Finally the behavior for non-monotonic loading is exemplary investigated. The previous discussed set-up with variable interface direction and "relaxed" boundary conditions is used up to a deformation of $F_{33} = 1.05$. Afterwards the sample is deformed by $F_{13} = 0.02$ simple shear using the boundary conditions explained in Section 4. Fig. 17 shows two representative stress components for this non-monotonic loading path. The results for S_{33} are in accordance to the previous results for the von Mises stress up to $F_{33} = 1.05$. As the shear deformation starts a decrease of this stress component can be observed. The laminate model (S_{33}-laminate) shows in general the same tendency as the investigated real structure (S_{33}-real), however, the stress decrease is higher for the real structure, resulting form the complex microstructure. The stress component S_{13} is in the laminate model for F_{33} negligible whereas the real structure shows a non-negligible S_{13} value as a result of the complex interaction between soft and hard phase. For F_{13} loading the S_{13} component shows for both models a qualitative similar behavior. As this exemplary investigation indicates, the laminate model is also able to show the correct qualitative behavior for a non-monotonic loading path.

In general the homogenized laminate and the microstructural model show qualitatively similar stress–strain results, especially

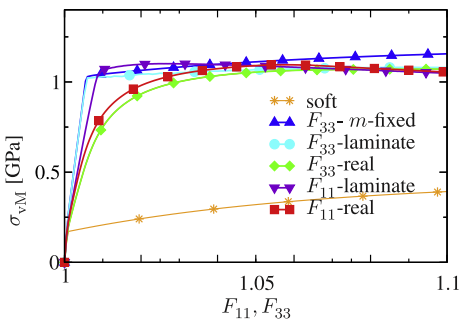

Fig. 16. Comparison of stress–strain behavior for "relaxed" boundary conditions of laminate model with fixed and variational m for $\lambda = 0.63$ with $\beta = 0.095$ and $m_{\text{initial}} = \{100\}$ under compression and extension with microstructural model.

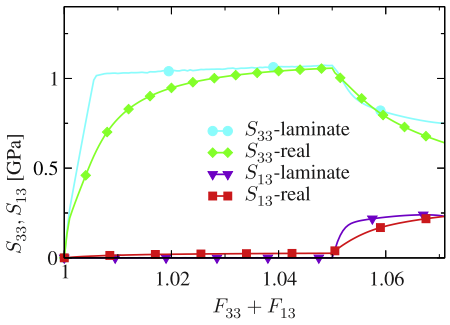

Fig. 17. Comparison of stress–strain behavior for non-monotonic loading for "relaxed" boundary conditions of laminate model with variational m for $\lambda = 0.63$ with $\beta = 0.095$ and $m_{\text{initial}} = \{100\}$ under extension and shear with microstructural model.

for "hard" boundary conditions which are more relevant here due to avoid phenomena like necking. The calculation time is much less for the laminate model compared to the microstructural model which is important for technological simulations like a roller burnishing process (e.g., Wiederkehr et al., 2011).

8. Discussion and conclusions

As mentioned in previous sections, in a more realistic approach, brittle failure would have to be included in the model for the hard phase. To get a first impression how the model behaves, a computation is done according to the loading cases in Fig. 3. To model the behavior of brittle failure and the resulting softening the material parameters are chosen as displayed in Table 1, but changing the parameters for the hard phase to $s_H = -1870$ MPa and $c_H = 100$. The resulting behavior is shown in Fig. 18. The differences for the extension and compression load case are clearly visible. Due to the lower amount of deformation for the hard phase in the compression case as in the extension case (see Fig. 4) it takes more overall deformation until the softening begins. Up to this point the soft phase was subjected to deformation which leads to an inelastic behavior with resulting hardening. Therefore the differences in the effective yield stress as well as strain are higher for the two deformation cases in contrast to ideal viscoplasticity.

In this work, we have investigated the application of first-order laminate theory as a homogenization ansatz to model the inelastic behavior of thin-coating-like or thin-film-like two-phase composites whose microstructural morphology is characterized by being layered or lamellar in nature. This approach has been developed

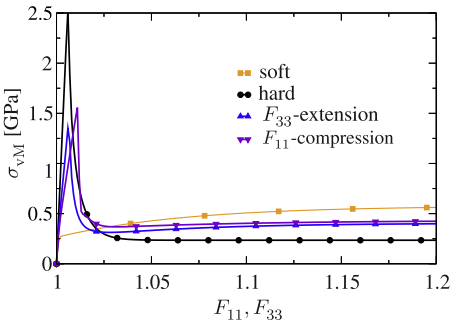

Fig. 18. Macroscopic von Mises stress σ_{vM} in the composite subject to different normal deformation conditions as a function of F_{11} (compression) or F_{33} (extension) for soft-phase volume fraction of $\lambda = 0.5$. The material parameters of the hard phase are changed to $s_H = -1870$ MPa and $c_H = 100$. Also shown for comparison is the behavior of the pure hard (solid circles), modeled with softening behavior and pure soft (solid squares) for either extension or compression.

and compared with a number of existing homogenization methods as well as with finite-element (FE) models for ideal and real microstructures. The laminate-based homogenization model showed very good agreement with the ideal FE model for a number of different deformation conditions including extension, compression and shear. This was the case both for homogeneous and inhomogeneous deformation conditions. Additional comparisons were carried out with standard homogenization assumptions like those of Taylor, as well as with homogenization based on the assumption of phase-wise constant plastic strain (EPc). These comparisons show that the Taylor model predicts the behavior for extension quite well. On the other hand, the EPc model predicts the behavior well only for compression. The Sachs model is not appropriate in any of these cases.

A first extension of this model is presented where the interface normal $\boldsymbol{m}$ is variable within the limits of a cone around the initial orientation, which can physically interpreted as an interface stiffness. In the last part of the work, the laminate homogenization models with and without variable interface normal $\boldsymbol{m}$ are compared to FE-models based on real discretized micrographs which show a laminate structure. It was shown that both models show a qualitative similar behavior.

For simplicity, the hard phase of the model microstructures considered in this work was treated as thermoelastic, ideal viscoplastic in nature, with elastic and yield properties significantly larger than those of the soft phase. It would be more realistic to model this phase as thermoelastic and brittle. Furthermore the reorientation of the interface is modeled purely energetic in nature. More generally, one could expect inelastic/kinetic/dissipative processes to influence the orientation of the interface. These generalizations of the current laminate-based approach, along with the application of the approach to the modeling and simulation of the compaction of thermally-sprayed coatings, represent work in progress, and will be reported on in the future.

Acknowledgement

Partial financial support for this work provided by the German Science Foundation (DFG) under contract SFB 708 is gratefully acknowledged.

References

Agoras, M., Ponte Castañeda, P., 2011. Homogenization estimates for multi-scale nonlinear composites. European Journal of Mechanics – A/Solids 30 (6), 828–843.

Ahzi, S., Bahlouli, N., Makradi, A., Belouettar, S., 2007. Composite modeling for the effective elastic properties of semicrystalline polymers. Journal of Mechanics of Materials and Structures 2 (1), 1–22.

Ahzi, S., Parks, D., Argon, A., 1990. Modeling of plastic deformation evolution of anisotropy in semi-crystalline polymers. In: American Society of Mechanical Engineers, Materials Division (Publication) MD, vol. 20, pp. 287–292.

Ahzi, S., Parks, D.M., Argon, A.S., 1995. Estimates of the overall elastic properties in semi-crystalline polymers. In: American Society of Mechanical Engineers, Applied Mechanics Division, AMD, vol. 203, pp. 31–40.

Bargmann, S., Ekh, M., Runesson, K., Svendsen, B., 2010. Modeling of polycrystals with gradient crystal plasticity: a comparison of strategies. Philosophical Magazine 90 (10), 1263–1288.

Benveniste, Y., 1987. A new approach to the application of Mori–Tanaka's theory in composite materials. Mechanics of Materials 6 (2), 147–157.

Böhlke, T., Risy, G., Bertram, A., 2008. A micro-mechanically based quadratic yield condition for textured polycrystals. ZAMM Zeitschrift fur Angewandte Mathematik und Mechanik 88 (5), 379–387.

Christensen, R.M., Lo, K.H., 1979. Solutions for effective shear properties in three phase sphere and cylinder models. Journal of the Mechanics and Physics of Solids 27 (4), 315–330.

Drugan, W.J., Willis, J.R., 1996. A micromechanics-based nonlocal constitutive equation and estimates of representative volume element size for elastic composites. Journal of the Mechanics and Physics of Solids 44 (4), 497–524.

Du, D., Zheng, Q., 2002. A further exploration of the interaction direct derivative (IDD) estimate for the effective properties of multiphase composites taking into account inclusion distribution. Acta Mechanica 157, 61–80.

Dvorak, G., 1992. Transformation field analysis of inelastic composite materials. Proceedings of the Royal Society of London A 437, 311–326.

Dvorak, G., Bahei-El-Din, Y., Wafa, A., 1994a. The modeling of inelastic composite materials with the transformation field analysis. Modelling and Simulation in Materials Science and Engineering 2 (3A), 571.

Dvorak, G.J., Wafa, A.M., Bahei-El-Din, Y.A., 1994b. Implementation of the transformation field analysis for inelastic composite materials. Computational Mechanics 14, 201–228.

Eshelby, J.D., 1957. The determination of the elastic field of an ellipsoidal inclusion, and related problems. Proceedings of the Royal Society of London 241 (1226), 376–396.

Feyel, F., 2003. A multilevel finite element method (FE2) to describe the response of highly non-linear structures using generalized continua. Computer Methods in Applied Mechanics and Engineering 192 (28-30), 3233–3244.

Forest, S., 2008. Some links between cosserat, strain gradient crystal plasticity and the statistical theory of dislocations. Philosophical Magazine 88 (30), 3549–3563.

Fritzen, F., Böhlke, T., 2010. Three-dimensional finite element implementation of the nonuniform transformation field analysis. International Journal for Numerical Methods in Engineering 84 (7), 803–829.

Fritzen, F., Böhlke, T., 2011. Nonuniform transformation field analysis of materials with morphological anisotropy. Composites Science and Technology 71 (4), 433–442.

Fülöp, T., Brekelmans, W., Geers, M., 2006. Size effects from grain statistics in ultra-thin metal sheets. Journal of Materials Processing Technology 174 (1-3), 233–238.

Geers, M., Kouznetsova, V., Brekelmans, W., 2010. Multi-scale computational homogenization: trends and challenges. Journal of Computational and Applied Mathematics 234 (7), 2175–2182.

Gross, D., Seelig, T., 2006. Fracture Mechanics: With an Introduction to Micromechanics, first ed. Springer, Berlin, Heidelberg.

Han, D., Mecholsky Jr., J.J., 1990. Strength and toughness degradation of tungsten Carbide–Cobalt due to thermal shock. Journal of the American Ceramic Society 73 (12), 3692–3695.

Houtte, P.V., Li, S., Seefeldt, M., Delannay, L., 2005. Deformation texture prediction: from the Taylor model to the advanced lamel model. International Journal of Plasticity 21 (3), 589–624.

Jain, A., 1989. Fundamentals of Digital Image Processing, first ed. Prentice-Hall, Englewood Cliffs.

Jänicke, R., Diebels, S., Sehlhorst, H., Düster, A., 2009. Two-scale modelling of micromorphic continua: a numerical homogenization scheme. Continuum Mechanics and Thermodynamics 21 (4), 297–315.

Kanit, T., Forest, S., Galliet, I., Mounoury, V., Jeulin, D., 2003. Determination of the size of the representative volume element for random composites: statistical and numerical approach. International Journal of Solids and Structures 40 (13-14), 3647–3679.

Klusemann, B., 2010. Application of homogenization methods and crystal plasticity to the modeling of heterogenous materials of technological interest. Ph.D. thesis, Schriftenreihe des Instituts für Mechanik Nr. 2, TU Dortmund University, Germany.

Klusemann, B., Bargmann, S., Svendsen, B., 2012a. Two models for gradient inelasticity based on non-convex energy. Computational Materials Science. http://dx.doi.org/10.1016/j.commatsci.2012.01.037.

Klusemann, B., Böhm, H., Svendsen, B., 2012b. Homogenization methods for multi-phase elastic composites with non-elliptical reinforcements: comparisons and benchmarks. European Journal of Mechanics – A/Solids 34, 21–37.

Klusemann, B., Denzer, R., Svendsen, B., 2012c. Microstructure based modeling of residual stresses in WC-12Co sprayed coatings. Journal of Thermal Spray Technology 21 (1), 96–107.

Klusemann, B., Svendsen, B., Vehoff, H., 2012d. Investigation of the deformation behavior of Fe3%Si sheet metal with large grains via crystal plasticity and finite-element modeling. Computational Materials Science 52 (1), 25–32.

Kouznetsova, V., Balmachnov, A., Geers, M., 2009. A multi-scale model for structure–property relations of materials exhibiting martensite transformation plasticity. International Journal of Material Forming 2 (0), 491–494.

Kouznetsova, V., Geers, M., Brekelmans, W., 2004. Multi-scale second-order computational homogenization of multi-phase materials: a nested finite element solution strategy. Computer Methods in Applied Mechanics and Engineering 193 (48–51), 5525–5550.

Langer, S.A., Fuller, E.R., Carter, W.C., 2001. OOF: an image-based finite-element analysis of material microstructures. Computing in Science and Engineering 3 (3), 15–23.

Lebensohn, R., Tome, C., 1993. A self-consistent anisotropic approach for the simulation of plastic deformation and texture development of polycrystals: application to zirconium alloys. Acta Metallurgica et Materialia 41 (9), 2611–2624.

Lee, B., Argon, A., Parks, D., Ahzi, S., Bartczak, Z., 1993a. Simulation of large strain plastic deformation and texture evolution in high density polyethylene. Polymer 34 (17), 3555–3575.

Lee, B.J., Ahzi, S., Asaro, R.J., 1995. On the plasticity of low symmetry crystals lacking five independent slip systems. Mechanics of Materials 20 (1), 1–8.

Lee, B.J., Ahzi, S., Parks, D.M., 2002. Bicrystal-Based modeling of plasticity in FCC metals. Journal of Engineering Materials and Technology 124 (1), 27–40.

Lee, B.J., Parks, D.M., Ahzi, S., 1993b. Micromechanical modeling of large plastic deformation and texture evolution in semi-crystalline polymers. Journal of the Mechanics and Physics of Solids 41 (10), 1651–1687.
Mercier, S., Molinari, A., 2009. Homogenization of elastic–viscoplastic heterogeneous materials: self-consistent and Mori–Tanaka schemes. International Journal of Plasticity 25 (6), 1024–1048.
Michel, J., Suquet, P., 2003. Nonuniform transformation field analysis. International Journal of Solids and Structures 40 (25), 6937–6955.
Michel, J., Suquet, P., 2004. Computational analysis of nonlinear composite structures using the nonuniform transformation field analysis. Computer Methods in Applied Mechanics and Engineering 193 (48-51), 5477–5502.
Miehe, C., Schotte, J., Schrder, J., 1999. Computational micro‘‘macro transitions and overall moduli in the analysis of polycrystals at large strains. Computational Materials Science 16 (1–4), 372–382.
Molinari, A., Ahzi, S., Kouddane, R., 1997. On the self-consistent modeling of elastic–plastic behavior of polycrystals. Mechanics of Materials 26 (1), 43–62.
Molinari, A., Canova, G., Ahzi, S., 1987. A self consistent approach of the large deformation polycrystal viscoplasticity. Acta Metallurgica 35 (12), 2983–2994.
Monetto, I., Drugan, W., 2009. A micromechanics-based nonlocal constitutive equation and minimum RVE size estimates for random elastic composites containing aligned spheroidal heterogeneities. Journal of the Mechanics and Physics of Solids 57 (9), 1578–1595.
Monetto, I., Drugan, W.J., 2004. A micromechanics-based nonlocal constitutive equation for elastic composites containing randomly oriented spheroidal heterogeneities. Journal of the Mechanics and Physics of Solids 52 (2), 359–393.
Moulinec, H., Suquet, P., 1998. A numerical method for computing the overall response of nonlinear composites with complex microstructure. Computer Methods in Applied Mechanics and Engineering 157 (1–2), 69–94.
Nemat-Nasser, S., Hori, M., 1993. Bounds and estimates of overall moduli of composites with periodic microstructure. Mechanics of Materials 15 (3), 163–181.
Nemat-Nasser, S., Hori, M., 1999. Micromechanics: Overall Properties of Heterogeneous Materials, second ed. Elsevier, Amsterdam.
Okamoto, S., Nakazono, Y., Otsuka, K., Shimoitani, Y., Takada, J., 2005. Mechanical properties of WC/Co cemented carbide with larger WC grain size. Materials Characterization 55 (4–5), 281–287.
Ortiz, M., Repetto, E.A., Stainier, L., 2000. A theory of subgrain dislocation structures. Journal of the Mechanics and Physics of Solids 48 (10), 2077–2114.
Pahr, D., Zysset, P., 2008. Influence of boundary conditions on computed apparent elastic properties of cancellous bone. Biomechanics and Modeling in Mechanobiology 7, 463–476.
Parks, D.M., Ahzi, S., 1990. Polycrystalline plastic deformation and texture evolution for crystals lacking five independent slip systems. Journal of the Mechanics and Physics of Solids 38 (5), 701–724.
Pierard, O., Friebel, C., Doghri, I., 2004. Mean-field homogenization of multi-phase thermo-elastic composites: a general framework and its validation. Composites Science and Technology 64 (10–11), 1587–1603.
Ponte Castañeda, P., 1991. The effective mechanical properties of nonlinear isotropic composites. Journal of the Mechanics and Physics of Solids 39 (1), 45–71.
Ponte Castaneda, P., Suquet, P., 1998. Nonlinear composites. Advances in Applied Mechanics 34, 107–301.
Reid, A.C., Langer, S.A., Lua, R.C., Coffman, V.R., Haan, S., Garcia, R.E., 2008. Image-based finite element mesh construction for material microstructures. Computational Materials Science 43 (4), 989–999.
Roussette, S., Michel, J., Suquet, P., 2009. Nonuniform transformation field analysis of elastic viscoplastic composites. Composites Science and Technology 69 (1), 22–27.
Sachs, G., 1928. Plasticity problems in metals. Zeitschrift des Vereines deutscher Ingenieure 72, 734–736.
Silhavy, M., 1997. The Mechanics and Thermodynamics of Continuous Media, first ed. Springer-Verlag, Berlin.
Smit, R., Brekelmans, W., Meijer, H., 1998. Prediction of the mechanical behavior of nonlinear heterogeneous systems by multi-level finite element modeling. Computer Methods in Applied Mechanics and Engineering 155, 181–192.
Taylor, G., 1938. Plastic strains in metals. Journal of the Institute of Metals 62, 307–324.
Tillmann, W., Klusemann, B., Nebel, J., Svendsen, B., 2011. Analysis of the mechanical properties of an Arc-Sprayed WC–FeCSiMn coating: nanoindentation and simulation. Journal of Thermal Spray Technology 20 (1), 328–335.
Torquato, S., Lado, F., 1992. Improved bounds on the effective elastic moduli of random arrays of cylinders. Journal of Applied Mechanics 59 (1), 1–6.
van Dommelen, J.A.W., Parks, D.M., Boyce, M.C., Brekelmans, W.A.M., Baaijens, F.P.T., 2003. Micromechanical modeling of the elasto-viscoplastic behavior of semi-crystalline polymers. Journal of the Mechanics and Physics of Solids 51 (3), 519–541.
Wiederkehr, T., Klusemann, B., Gies, D., Müller, H., Svendsen, B., 2010. An image morphing method for 3d reconstruction and fe-analysis of pore networks in thermal spray coatings. Computational Materials Science 47 (4), 881–889.
Wiederkehr, T., Klusemann, B., Müller, H., Svendsen, B., 2011. Fast, curvature-based prediction of rolling forces for porous media based on a series of detailed simulations. Advances in Engineering Software 42 (4), 142–150.
Zaoui, A., 1970. Thèse de doctorat distribution continue de dislocations: Théorie générale et quelques applications. Ph.D. thesis, Université de Paris, France.
Zheng, Q.S., Du, D.X., 2001. An explicit and universally applicable estimate for the effective properties of multiphase composites which accounts for inclusion distribution. Journal of the Mechanics and Physics of Solids 49 (11), 2765–2788.